Magnetic domain structure of ferromagnetic Tb(0001) films

Patrick Härtl [1,*], Markus Leisegang [1], and Matthias Bode [1,2]

[1] *Physikalisches Institut, Experimentelle Physik II, Universität Würzburg, Am Hubland, 97074 Würzburg, Germany*

[2] *Wilhelm Conrad Röntgen-Center for Complex Material Systems (RCCM), Universität Würzburg, Am Hubland, 97074 Würzburg, Germany*

(Received 11 July 2024; accepted 28 October 2024; published 12 November 2024)

We present the results of a spin-polarized scanning tunneling microscopy study performed on epitaxial Tb(0001) films grown on W(110). The magnetic contrast was obtained by dipping the tip directly into the Tb film, thereby creating magnetic in-plane sensitive tips. Our differential conductance dI/dU data reveal contrast levels which are in agreement with the tunneling magnetoresistance effect between an in-plane sensitive scanning tunneling microscopy tip and surface domains magnetized along basal $\langle 10\bar{1}0\rangle$ directions. Film-thickness-dependent studies reveal a close correlation between the structural and magnetic properties of the film. Four types of crystal defects are identified which contribute to the pinning of magnetic domains: (i) surface step edges, (ii) step dislocations, (iii) structural boundaries between differently stacked terbium (Tb) patches, and (iv) screw dislocations resulting from glide processes. As the thickness of the Tb film increases, the defect density diminishes, leading to the formation of larger domains. A detailed analysis of the domain walls leads to the conclusion that they are of Néel type and exhibit a width of $w_{60} \approx 1.4$ nm, $w_{120} \approx 2.5$ nm, and $w_{180} \approx 3$ nm for 60°, 120°, and 180° domain walls, respectively.

DOI: 10.1103/PhysRevB.110.184405

I. INTRODUCTION

The functionality of numerous devices relies on the magnetic properties of rare-earth metals (REMs), a group of 15 elements with increasing $4f$-shell occupation. While the $4f$ shells of lanthanum, ytterbium, and lutetium are either completely empty or filled, the partially filled $4f$ shells of the remaining 12 REMs carry a sizable Hund's rule magnetic moment and bears the potential for long-range magnetic order. Indeed, the magnetic properties and spin structures of REM bulk materials were intensively investigated by neutron scattering experiments in the 1950s and 1960s [1,2]. In contrast, our knowledge of their surface magnetic domain structure is surprisingly sparse. The main reason for this fact lies in the high chemical reactivity of REMs which makes the proper cleaning of surfaces of bulk crystals virtually impossible [3,4].

To circumvent these complications, single-crystalline epitaxial REM films have usually been grown on suitable refractory substrates, mostly W(110). Spin-polarized scanning tunneling microscopy (SP-STM) studies [5,6] of such high-quality REM films enable the real-space mapping of complex magnetic domain structures with unparalleled surface sensitivity and atomic-scale resolution. Utilizing this technique, the surface magnetic structures of a few REMs, i.e., dysprosium (Dy) [7–9], gadolinium (Gd) [10,11], and neodymium (Nd) [12], have been imaged and systematically investigated. For Gd ($4f^7$) films, Härtl *et al.* [11] observed a thickness-dependent spin-reorientation transition at around 100 atomic layers (AL), where the easy magnetization axis rotates from in-plane in thinner films to out-of-plane in thicker films. In contrast, for Dy ($4f^{10}$) films, Berbil-Bautista *et al.* [8] found ferromagnetic in-plane order with sixfold symmetry in the entire studied thickness regime between 14 and 500 AL. A detailed analysis revealed that the domain walls are of Néel type [8]. On the light REM Nd ($4f^4$), Kamber *et al.* [12] conducted a temperature- and magnetic-field-dependent SP-STM study, demonstrating spin-glass-like behavior. Despite these intriguing discoveries, the surface spin structures of 9 out of 12 rare-earth metals remain uncharted.

For terbium (Tb), the topic of our study, several studies performed with various measurement techniques can be found in the literature [13–26]. Tb crystallizes in the hexagonal close-packed (hcp) crystal structure with properties similar to those of the neighboring heavy REMs Gd and Dy (see, e.g., Sec. 1.3 in Ref. [27] for further information). Despite their structural similarities, the heavy REMs exhibit a variety of bulk magnetic properties [2]. For bulk Tb, which carries a magnetic moment of 9.34 μ_B per atom, two magnetic phases were identified. Below $T_C = 220$ K, it is ferromagnetic [28]. In a narrow temperature range, i.e., between $T_C = 220$ K and $T_N = 228$ K, a compensated magnetic structure—often called "antiferromagnetic"—has been found, which is better described by ferromagnetically ordered basal planes which exhibit a helical magnetic structure along the c axis [2,29].

Tb exhibits a large magnetic anisotropy which originates from the coupling of the angular moment ($L = 3$) to the spin moment of the partially filled $4f$ shell, accompanied by a low-symmetry crystalline electric field (nonspherical charge distribution) [25,30]. The hard magnetization axis is along the c axis, i.e., along the [0001] direction. Within the basal plane, higher-order anisotropy terms energetically favor a magnetization oriented along the b axes ($\langle 10\bar{1}0\rangle$ directions), whereas the a axes ($\langle 11\bar{2}0\rangle$ directions) represent the hard axis within the basal plane at all temperatures [2,23,25,29,31–33]. Due to the sixfold symmetry of the (0001) plane, six equivalent

*Contact author: patrick.haertl@uni-wuerzburg.de

magnetization directions are possible. The surface electronic properties of Tb(0001)/W(110) films are governed by a $5d_{z^2}$-like surface state which is split in an occupied majority and an empty minority spin part [17] at low temperatures, exhibiting binding energies of (-135 ± 8) and $(+430 \pm 15)$ meV [21], respectively. A spin-polarized low-energy electron microscope (SPLEEM) investigation [25] performed on Tb films on W(110) with a thickness of 20 atomic layers (AL) found unexpectedly large domain sizes that were reported to reach "several micrometers along the preferential step orientation." However, this surprising outcome was potentially ascribed to the limited resolution of SPLEEM which could lead to an "average of smaller domains with different orientations" [25].

To shed light on the magnetic domain structure of Tb(0001) films epitaxially grown on W(110), we here present a SP-STM study performed at low temperatures. We demonstrate that magnetically sensitive STM tips can be obtained by bringing the tip in contact with the Tb film. Utilizing such magnetized tips, we observe a sizable tunneling magnetoresistance (TMR) effect with discrete magnetic contrast levels. Hereby, the magnetic contribution to the differential conductance is proportional to the projection of the local sample magnetization onto the tip magnetization direction, as expected for SP-STM [5]. Maps of magnetic domain structures show that the domain size increases with film thickness. Correlation of topographic and magnetic data reveals that the domains are strongly pinned by defects, the density of which decreases with increasing film thickness. The domain walls between Tb domains are identified as Néel type with widths ranging from 1.4 to 4 nm.

II. EXPERIMENTAL SETUP AND PROCEDURES

The SP-STM experiments were conducted in a two-chamber ultrahigh vacuum (UHV) system at a base pressure of $p \leqslant 1 \times 10^{-10}$ mbar. The system consists of two separate UHV chambers, a preparation chamber and a chamber for cryogenic STM. In the preparation chamber, tips and samples can be treated on an electron-beam heating stage at temperatures well above 2300 K. With controllable leak valves, high-purity gases can be dosed into the preparation chamber. Furthermore, the preparation chamber is equipped with a home-built electron beam evaporator for Tb deposition. Immediately after preparation, samples are transferred *in vacuo* into the STM chamber. It is equipped with a bath cryostat cooled by liquid helium which contains a home-built STM operated at a base temperature $T_{\mathrm{STM}} \approx 4.5$ K.

Epitaxial Tb films with thicknesses ranging from $\Theta = 20$ AL to $\Theta = 500$ AL were deposited onto a W(110) substrate by following a very similar procedure as already described in Ref. [11] for Gd films. In a first step, the W(110) single crystal was cleaned in an oxygen atmosphere by a two-step flashing procedure with consecutive low-temperature ($T_{\mathrm{sample}} \approx 1200$ K) and high-temperature ($T_{\mathrm{sample}} \gtrsim 2200$ K) flashes [34]. For subsequent preparations, only single high-temperature flashes $T_{\mathrm{sample}} \gtrsim 2000$ K were needed to clean the crystal. To obtain clean Tb films, distilled Tb lumps (MaTeck, purity 99.9%, main impurities 200 ppm Fe and 900 ppm O) were at first melted in a Mo crucible. After extensive degassing, the chamber pressure during Tb evaporation did not exceed $p = 1 \times 10^{-9}$ mbar. Tb was deposited onto the clean W(110) substrate held at room temperature. As is shown below, we obtained continuous and flat Tb films by subsequent annealing for 5 min at $T_{\mathrm{ann}} \approx (950 \pm 100)$ K on the electron-beam heating stage (see Ref. [33] for details regarding optimal Tb growth parameters). As already described in Ref. [11], the *absolute* Tb deposition rate was determined by overview STM scans to evaluate the volume of Stranski-Krastanov grown films. For the parameters used throughout this study the Tb deposition rate amounted to (9.4 ± 0.7) AL per minute. We would like to emphasize that the relatively large error margin results from the statistical uncertainty associated with the limited STM scan range which allowed us to image a few islands only. We expect a much lower *relative* error between samples with different Tb coverages, as they are achieved by a simple scaling of the deposition time.

In our home-built cryogenic STM, the bias voltage U_{bias} is applied to the sample, i.e., negative (positive) bias voltages probe occupied (empty) electronic states of the sample. By applying a small modulation $U_{\mathrm{mod}} = 10$ mV to U_{bias}, the dI/dU map can be detected simultaneously with the constant-current image (topography) via the lock-in technique. To highlight structural details of our STM data, the z signal of all topographic constant-current images was augmented by its derivative with respect to the fast-scan direction, dz/dx. Further details can be found in Sec. II of the Supplemental Material of Ref. [11]. STM tips were electrochemically etched *ex situ* from polycrystalline tungsten wires and treated with high-temperature flashes ($T_{\mathrm{tip}} \geqslant 2200$ K) *in situ* to remove leftover contaminants. For magnetically sensitive SP-STM measurements, the procedure originally described in Refs. [8,11] was employed. In our case the STM tip was either gently dipped a few nanometers into the Tb film or pulsed at voltages of $U_{\mathrm{bias}} \geqslant \pm 6$ V. Both procedures reliably led to a strong TMR effect [5]. Similar to previous studies on Dy [8] and Gd [11], the strongest and most reliable contrast of such dip-coated rare-earth metal tips was found at bias voltages around $U_{\mathrm{bias}} \approx -900$ mV. Therefore, the dI/dU maps presented in this study were obtained at this bias voltage. We speculate that the contrast is related to the Δ_2-symmetric minority $2\uparrow$ band of Tb which disperses in the ΓM and ΓK directions (see Fig. 2 in Ref. [23]).

III. RESULTS

A. Domain evaluation

Hexagonal surfaces like Tb(0001) typically exhibit six crystallographically equivalent easy magnetization directions $\vec{m}_{\mathrm{s}}$, sketched as gray arrows with an angle of 60° towards each other in Figs. 1(a)–1(c). Since the TMR effect scales with the cosine of the angle α between the magnetization direction of the two electrodes [35,36], the TMR-derived SP-STM contrast is given by the projection of the local sample magnetization $\vec{m}_{\mathrm{s}}$ onto the tip magnetization $\vec{m}_{\mathrm{t}}$ [8,37]. Restricting ourself to in-plane orientations of the magnetic moment—a situation not only justified by the abovementioned large basal anisotropy but also by the results of this study discussed below—three general cases, schematically presented in Fig. 1, must be distinguished: (a) the tip magnetization lies along the

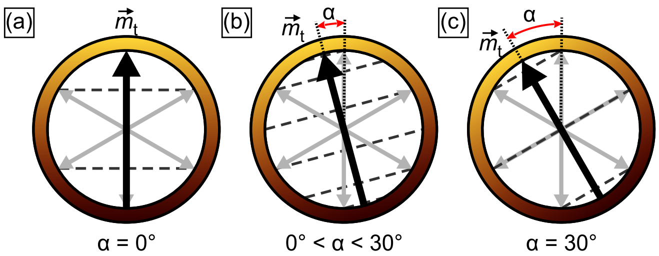

FIG. 1. Schematic representation of the possible relative orientations of the tip magnetization ($\vec{m}_t$, thick black arrows) to the easy magnetization directions ($\vec{m}_s$, thin gray arrows) of a sample with hexagonal crystal symmetry, like Tb(0001) on W(110). Since the TMR effect scales with the projection of $\vec{m}_s$ onto $\vec{m}_t$ (thin hatched lines), three cases can be distinguished. The determining parameter is the azimuthal angle α between $\vec{m}_t$ and the nearest sample magnetization direction: (a) $\alpha = 0^\circ$, where $\vec{m}_t$ is aligned along one high-symmetry axis of the sample, results in four contrast levels. (b) $0^\circ < \alpha < 30^\circ$ leads to six and (c) $\alpha = 30^\circ$ to three different contrast levels.

easy axis, leading to four contrast levels; (b) for an angle between the in-plane easy and the in-plane hard axis, six contrast levels are expected; and (c) if the tip magnetization is pointing along the in-plane hard axis ($\alpha = 30^\circ$), only three different contrasts are observed. Exemplary experimental results demonstrating cases (b) and (c) are presented in the following.

The results obtained on two films measured with two microscopically different tips are displayed in Fig. 2. In the upper row, Fig. 2(a) shows the topography of a 90-AL Tb film. As reported previously in Refs. [25,33,38], Tb grows on W(110) in the Nishiyama-Wassermann epitaxial relation, i.e., Tb[$\bar{1}\bar{1}20$] ∥ W[$00\bar{1}$] and Tb(0001) ∥ W(110). The topography reveals slightly buckled terraces separated by step edges with monatomic height equivalent to half the c axis. These step edges are neither infinite nor parallel, as usually observed for pseudomorphic film growth [39]. Instead, each step edge—together with another step edge—appears and disappears at a double-screw dislocation, one of which is marked by a black circle in Fig. 2(a). Close inspection reveals that each double-screw dislocation is also the starting point of two buried step edges, marked by two arrows in Fig. 2(a), which cause the buckled appearance of the terraces. Overall, the topographic appearance is very similar to previous observations made for Dy [8] and Gd [11]. As described in these references in detail, the growth is characterized by the nucleation of differently stacked, hcp-ordered patches which release their structural domain boundaries above a critical thickness, resulting in both double-screw dislocations and buried step edges.

The magnetically sensitive dI/dU map presented in Fig. 2(b) shows a characteristic pattern with discrete dI/dU levels [40]. The existence of some dendritically shaped indentations signals a tiny (<3% of the surface area) hydrogen (H) contamination caused by a nonperfectly clean Tb source in the early days of this experimental study. These patches appear dark in the dI/dU map due to the lower density of states of H/Tb(0001), as already observed in earlier studies [11,41–44]. This is substantiated by the corresponding histogram presented in Fig. 2(c) which reveals six well-separated peaks labeled i–vi from lowest to highest intensity of the dI/dU signal. As explained above, the existence of six separate signal levels indicates an in-plane tip magnetization $\vec{m}_t$ which lies between an easy axis and an in-plane hard axis of the film [cf. Fig. 1(b)]; i.e., α must be within the range of $0^\circ < \alpha < 30^\circ$.

The distribution of contrast levels displayed in the histogram of Fig. 2(c) can be fitted by the sum (red line) of six Lorentzian functions (gray-shaded peaks labeled i–vi). The resulting peak positions of the experimentally measured differential conductance dI/dU_n^{exp} for domains $n = \text{i}, \ldots, \text{vi}$ are listed in the second column of Table I. As has been shown theoretically [37] and experimentally [8], the dI/dU_n^{exp} signal can be separated into a universal spin-averaged (dI/dU^{sa}) component and a domain-specific spin-polarized (dI/dU_n^{sp}) component:

$$\begin{aligned} dI/dU_n^{\text{exp}} &= dI/dU^{\text{sa}} + dI/dU_n^{\text{sp}} \\ &= dI/dU^{\text{sa}} + dI/dU^{\text{sp}} \cos(\alpha + \theta_n), \end{aligned} \tag{1}$$

where α is the before-mentioned angle between the magnetization direction of the tip $\vec{m}_t$ and sample magnetization closest to this direction, i.e., $\vec{m}_s$ of domain vi. θ_n denotes the angle between the wall normal and the tip magnetization $\vec{m}_t$ at $\theta_n = 0^\circ, -60^\circ, +60^\circ, -120^\circ, +120^\circ$, and 180° for $n = 1, \ldots, 6$, respectively. The spin-averaged component dI/dU^{sa} is determined by the arithmetic mean of all dI/dU_n^{exp} values listed in the second column of Table I, resulting in $dI/dU^{\text{sa}} = (6.59 \pm 0.01)$ arb. units for this particular tip.

The domain-specific spin-polarized components, given by $dI/dU_n^{\text{sp}} = dI/dU_n^{\text{exp}} - dI/dU^{\text{sa}}$, as derived from the Lorentzian fit of the histogram, are displayed in the third column of Table I. In the ideal scenario described by Eq. (1), oppositely magnetized domains, i.e., the domain pairs (i, vi), (ii, v), and (iii, iv), should exhibit the same absolute value of dI/dU_n^{sp}. Even though dI/dU_n^{sp} generally follows this trend, some deviations can be identified in Table I. We speculate that these deviations may be caused by a nonconstant tip-sample distance, resulting from the active feedback loop which keeps the tunneling current constant, or by local impurities with different electronic properties.

One possible relative orientation of $\vec{m}_t$ which would result in peak positions consistent with the observations is schematically sketched in the upper inset of Fig. 2(c), resulting in $\alpha = (21 \pm 10)^\circ$. Based on the experiments presented here, we are not able, however, to unambiguously determine the absolute magnetization directions of the tip and domains i–vi. For example, the situation sketched in the lower inset of Fig. 2(c) is also consistent with the data presented in Fig. 2(b) and the easy axis of Tb(0001). To distinguish the two cases sketched in the insets of Fig. 2(c) experimentally, a rotatable in-plane magnetic field would be required which is not available in our setup. Figure 2(d) shows the topography of a 100-AL Tb film grown on W(110), recorded with a microscopically different tip. It shows a comparable appearance as observed in Fig. 2(a). The simultaneously recorded dI/dU map and its histogram displayed in Figs. 2(e) and 2(f), respectively, reveal that this magnetic tip produces only three contrast levels. This result is expected for a tip which exhibits a magnetization that is rotated by an angle $\alpha = 30^\circ$ with respect to an easy axis of the

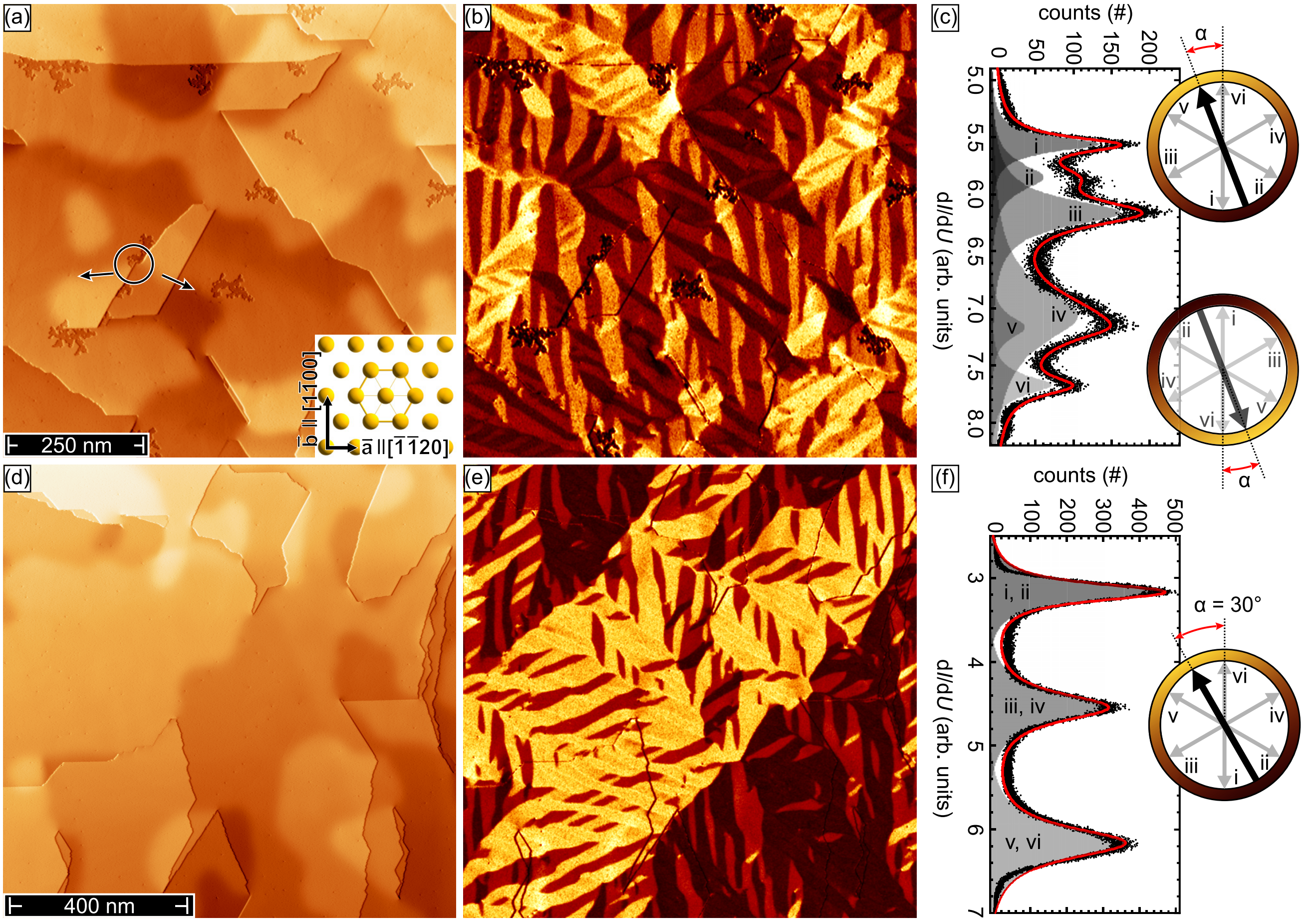

FIG. 2. (a) Topography and (b) simultaneously recorded dI/dU map for a 90-AL Tb film epitaxially grown on W(110). The inset in panel (a) displays the hcp unit cell with the according axes $[1\bar{1}00]$ and $[\bar{1}\bar{1}20]$. (c) Histogram of the dI/dU map in panel (b) (black dots) with a six-peak Lorentzian fit in red. (d)–(f) Same representation as in panels (a)–(c), but now for a 100-AL Tb film and a different tip magnetization $\vec{m}_t$, leading to only three magnetic contrast levels. Scan parameters: $U_{bias} = -900$ mV and $I_{set} = 1$ nA.

Tb surface, as discussed in Fig. 1(c) as well as in Ref. [8]. As shown in the inset of Fig. 2(f), the projections of certain pairs of domains onto the tip magnetization are identical: domains i and ii, domains iii and iv, and domains v and vi. Based on the well-ordered domain structure of Tb(0001)/W(110) films around 100 AL, a detailed analysis of the domain structure is possible. Figure 3 summarizes such an analysis of a specific dI/dU map obtained within a scan range of 250×250 nm^2. The inset indicates a possible orientation of the tip magnetization $\vec{m}_t$ (black arrow) with respect to the $\langle 10\bar{1}0\rangle$-oriented surface domains $n = $ i, ..., vi (gray arrows). Adjacent domains, such as the ones labeled i and ii, v and vi, or iii and v, are typically separated by 60° domain walls. For example, the domain marked with iv is largely surrounded by domain vi, corresponding to a 60° domain wall at the boundary. Only in the bottom left part of domain iv it adjoins to domain v, resulting in a 120° domain wall marked by a green ellipse. Two further occasions of 120° domain walls are indicated, and one 180° is marked by a blue ellipse. The domain profiles of 60°, 120°, and 180° domain walls is analyzed in detail in Sec. III C.

TABLE I. dI/dU analysis for the data presented in Figs. 2(b) and 2(c). With the spin-average part $dI/dU^{sa} = (6.59 \pm 0.01)$ arb. units and Eq. (1), the angle α of the tip magnetization $\vec{m}_t$ with respect to the sample magnetization direction $\vec{m}_s$ can be determined.

Domain No.	dI/dU_n^{exp} (arb. units)	dI/dU_n^{sp} (arb. units)
i	5.568 ± 0.004	-1.01 ± 0.01
ii	5.857 ± 0.002	-0.73 ± 0.01
iii	6.169 ± 0.001	-0.41 ± 0.01
iv	7.071 ± 0.005	$+0.48 \pm 0.01$
v	7.175 ± 0.002	$+0.59 \pm 0.01$
vi	7.680 ± 0.001	$+1.09 \pm 0.01$

B. Thickness-dependent domain structure

To understand the evolution of the thickness-dependent domain structure of epitaxially grown Tb(0001) films on W(110) substrates, we systematically studied the correlation of structural and magnetic properties over a wide film thickness range. A selection of typical results is presented in Fig. 4. The rows from top to bottom show SP-STM data of Tb films with thicknesses of (a)–(d) 20 AL, (e)–(h) 50 AL, (i)–(l) 100 AL, and (m)–(p) 500 AL. In each case the left column displays overview topography images and the right column displays the simultaneously recorded dI/dU maps revealing the corresponding magnetic domain structure. The two central columns

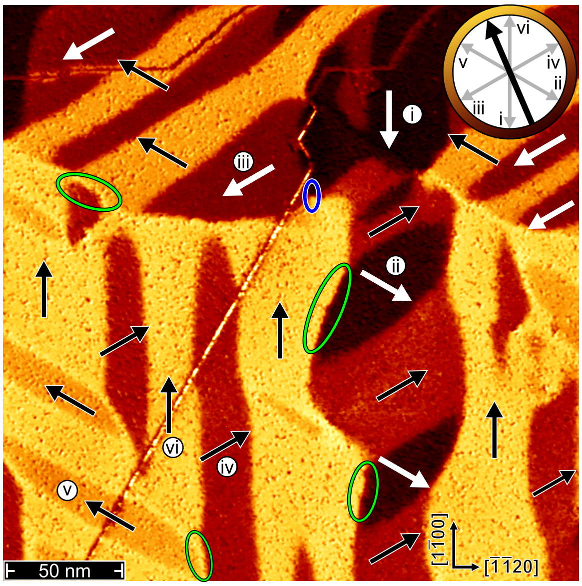

FIG. 3. Analysis of the relative tip to sample magnetization for the respective domain structure. The image presents the magnetic $\mathrm{d}I/\mathrm{d}U$ map of a 90-AL Tb film epitaxially grown on W(110). Black and white arrows indicate the orientation of the magnetization within the magnetic domains $\vec{m}_\mathrm{s}$ which is known to be along the $\vec{m}_\mathrm{s} = \langle 10\bar{1}0\rangle$ easy axis as reported in Ref. [25]. Their relative alignment with the tip magnetization (thick black arrow) is shown in the inset. Green (120°) and blue (180°) ellipses represent domain walls with a turn angle larger than 60°. Scan parameters: $U_\mathrm{bias} = -900$ mV and $I_\mathrm{set} = 1$ nA.

present detailed views of specific areas which are discussed in order to correlate structural and magnetic data.

The topography data show a thickness-dependent evolution of surface morphologies typical for rare-earth films deposited on bcc(110) surfaces [7,8,11]: For the 20-AL film shown in Fig. 4(a), a terrace-and-step structure is evident, with the underlying W steps still clearly visible. As the film thickness is increased to 50 AL [Fig. 4(e)], the positions of the underlying W step edges are no longer identifiable, and the film morphology has changed significantly. The surface now features numerous, short (<100 nm) step edges which always end in screw dislocations. Typically, the screw dislocations of two step edges merge at one point, giving rise to double-screw dislocations. Furthermore, a high density of smoothed-out step edges gives the STM image a cloudy appearance.

At 100 AL [Fig. 4(i)], the density of both the screw dislocations and the smoothed-out step edges is reduced significantly. Therefore, this Tb film appears much smoother. Increasing the film thickness to 500 AL [Fig. 4(m)] results in a further reduction of screw dislocations and the smoothed-out step edges. Especially in the lower part of Fig. 4(m) we find narrow terraces, possibly due to step bunching.

As evidenced by the magnetically sensitive $\mathrm{d}I/\mathrm{d}U$ maps displayed in the right column of Fig. 4, panels (d), (h), (l), and (p), this evolution of the surface morphology strongly influences the domain structure of Tb films. The 20-AL-thick film, Fig. 4(e), exhibits six distinct contrast levels, indicative of six in-plane magnetic domains [45]. Yet, the lateral size of these domains is very small, typically below 20 nm, i.e., much smaller than the terrace width observed for this sample in Fig. 4(a).

As highlighted by the magnified views in Figs. 4(b) and 4(c), the magnetic domain structure for 20-AL Tb on W(110) is strongly influenced by the structural properties of the film. Correlating structural and magnetic data, we find that three kinds of defects typically limit the lateral size of magnetic domains: (i) surface step edges (marked by an ellipses), (ii) step dislocations or impurities which appear as depressions in topographic STM scans (circles), and (iii) structural boundaries between differently stacked patches of hcp-Tb(0001) on W(110) which appear as trenches (white arrows). A close correlation between the position of the structural defects (i)–(iii) visible in Fig. 4(b) and the magnetic domain boundaries in Fig. 4(c) is eminent. Obviously, these structural defects act as pinning centers during the domain formation process when the sample is cooled through T_N and T_C, as described earlier for Dy(0001)/W(110) films [7]. Whether these structural features also result in magnetic pinning when driving the Tb films through a magnetic hysteresis may be explored in future experimental studies which involve external magnetic fields.

As the film thickness is increased to 50 AL, see Fig. 4(h), the typical domain size increases up to several 10 nm. The zoomed-in SP-STM data presented in Figs. 4(f) and 4(g) suggest that there is no detectable correlation between the positions of surface step edges and domain walls. Furthermore, the two surface defects which result from the relaxation of the structural domain boundaries between differently stacked Tb patches, i.e., double-screw dislocations and smoothed-out step edges, also less effectively pin magnetic domains. Only in few locations, two of which are marked by black arrows, the magnetic domains appear to be pinned by double-screw dislocations. The point-like depressions identified as edge dislocations or impurities remain the dominating pinning centers for domain walls. Some examples are marked by circles.

When increasing the thickness even further to 100 AL in Fig. 4(l), much larger domains appear with typical widths ranging from $w \approx 15, \ldots, 40$ nm and lengths of $l \approx 100, \ldots, 200$ nm. Hereby, the magnetic domains are elongated along the $\langle 10\bar{1}0\rangle$ directions, i.e., along the easy axis found in earlier studies [29,31]. Correlating the detailed topographic and magnetic $\mathrm{d}I/\mathrm{d}U$ map presented in Figs. 4(j) and 4(k), respectively, clearly shows that edge dislocations (circles), screw dislocations (black arrows), and the few remaining structural boundaries between differently stacked Tb patches (white arrows) remain effective pinning centers. However, the amount of structural defects is significantly reduced compared to the previous two lower Tb film thicknesses. For the thickest film presented in this study (500 AL), Fig. 4(p), the domain sizes increase further to $w \approx 50, \ldots, 90$ nm, and $l \approx 150, \ldots, 500$ nm. In films of this thickness, trenches from differently stacked patches [type (iii)] are no longer visible, and only a few screw dislocations remain. Yet, the point-like defects remain visible and still strongly pin the magnetic domains.

C. Domain wall analysis

As described for Fig. 3, different types of domain walls can be observed on Tb(0001)/W(110) films. In Fig. 5 we perform

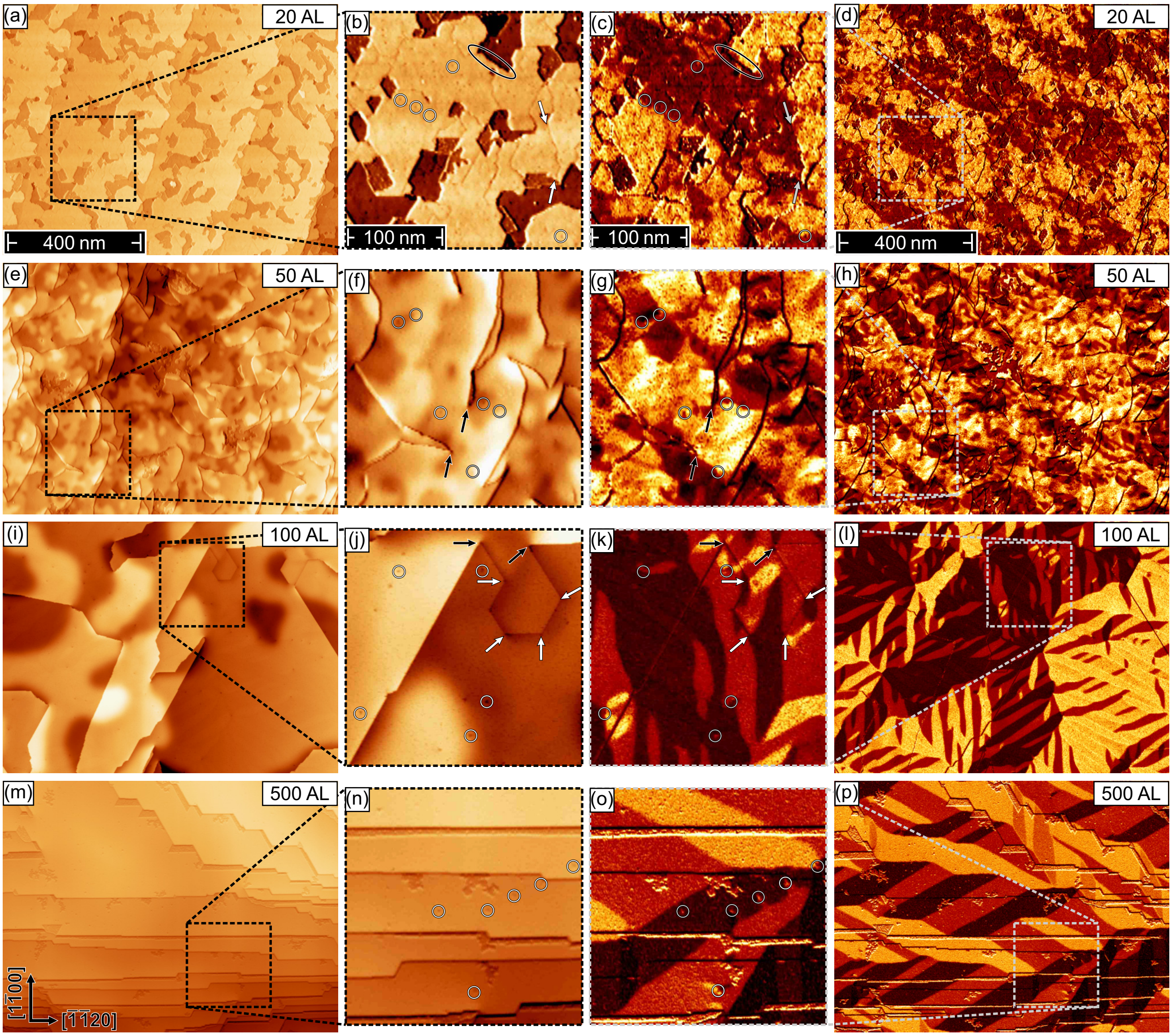

FIG. 4. Coverage-dependent structural (two left columns) and simultaneously recorded magnetic domain structures (two right columns) of Tb(0001) films on W(110) with thicknesses of (a)–(d) 20 AL, (e)–(h) 50 AL, (i)–(l) 100 AL, and (m)–(p) 500 AL. The middle two columns show zoom-in panels to illustrate the correlation between structural imperfections and the pining of magnetic domains. Scan parameters: $U_{\rm bias} = -900$ mV and $I_{\rm set} = 1$ nA.

a detailed analysis of typical domain wall profiles observed on a 90-AL film. Figure 5(a) displays the dI/dU map used for this analysis. Again, we observe six intensity levels which can be explained by the orientation of the particular tip magnetization $\vec{m}_{\rm t}$ indicated as a black arrow in the inset (see the Supplemental Material for a more detailed analysis [45]). As defined previously, the magnetization direction of domain vi is closest to $\vec{m}_{\rm t}$, whereas domain i is almost antiparallel.

We analyzed six different domain walls, highlighted by colored bars in Fig. 5(a). The line profiles show (b), (c) two 60° domain walls, (d), (e) two 120° domain walls, and (f), (g) two 180° domain walls. The respective plots also indicate, as light gray dashed horizontal lines, the domain-specific dI/dU values identified from the histogram of Fig. 5(a) [45].

Comparison of these lines with the data reveals, for example, that the profile of the 120° domain wall presented in Fig. 5(d) spans from domain ii to domain iii. On its trail, the local sample magnetization $\vec{m}_{\rm s}(x)$ hereby passes through level i which is almost antiparallel to the tip magnetization $\vec{m}_{\rm t}$. In contrast, the 120° domain wall profile plotted in Fig. 5(e) from domain iv to domain v passes through level vi almost parallel to $\vec{m}_{\rm t}$. As we see below, these different orientations of the sample magnetization $\vec{m}_{\rm s}$ in the wall center relative to the tip magnetization influence the measurement process and lead to slight variations of the measured domain wall width.

To achieve a quantitative evaluation of the experimental data, the line profiles which are shown as discrete points in Figs. 5(b)–5(g) were fitted with an analytical domain wall profile,

$$dI/dU(x) = dI/dU^{\rm sa} + dI/dU^{\rm sp}\cos(\varphi(x) + \theta), \quad (2)$$

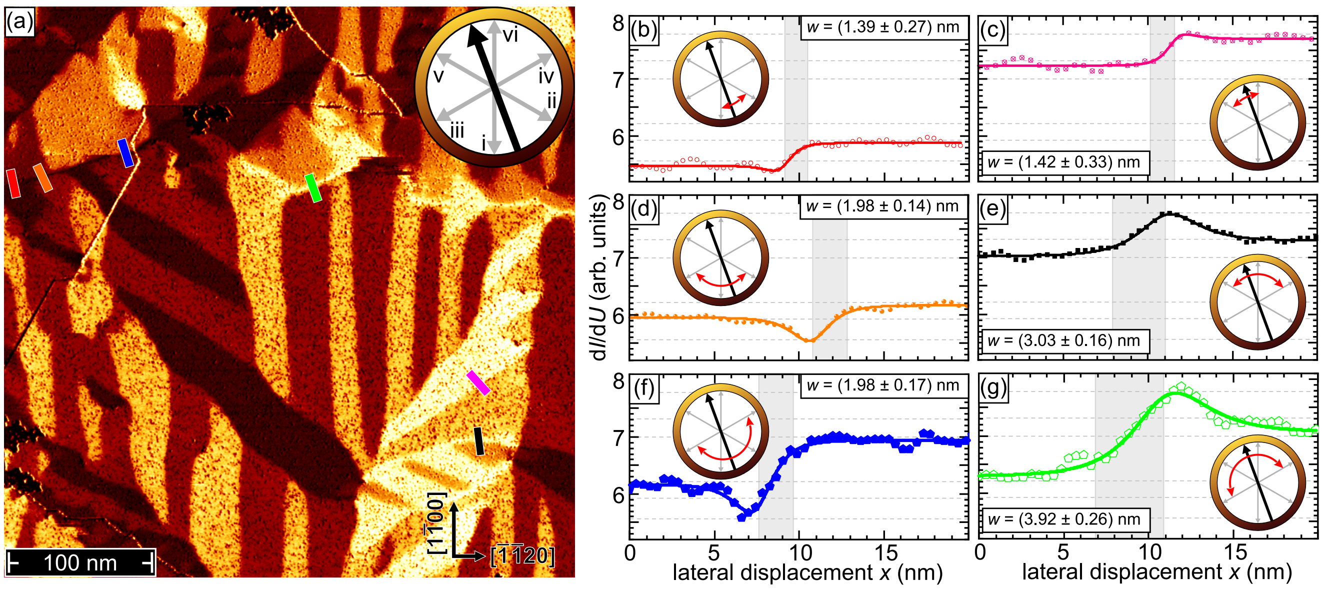

FIG. 5. Domain wall analysis of a 90-AL Tb/W(110) film. (a) $\mathrm{d}I/\mathrm{d}U$ signal revealing six different contrast levels, marked with i, …, vi from lowest to highest intensity. [(b)–(g)] Domain wall profiles $\mathrm{d}I/\mathrm{d}U(x)$ with the same color code as the lines drawn into panel (a), showing two 60° domain walls (wall widths $w_{60} \approx 1.4$ nm) in panels (b) and (c), two 120° domain walls ($w_{120} \approx 2$–3 nm) in panels (d) and (e), and two 180° domain walls ($w_{180} \approx 2$–4 nm) in panels (f) and (g). The insets reveal the relative orientations of $\vec{m}_\mathrm{t}$ onto $\vec{m}_\mathrm{s}$. Scan parameters: $U_\mathrm{bias} = -900$ mV and $I_\mathrm{set} = 1$ nA.

where $\mathrm{d}I/\mathrm{d}U^\mathrm{sa}$ and $\mathrm{d}I/\mathrm{d}U^\mathrm{sp}$ are the spin-averaged and spin-polarized contributions to the local differential conductance $\mathrm{d}I/\mathrm{d}U(x)$. θ and $\varphi(x)$ are the angles between the wall normal and the tip and the local sample magnetization, $\vec{m}_\mathrm{t}$ and $\vec{m}_\mathrm{s}(x)$, respectively. We describe the angle of the local sample magnetization by [8,46,47]

$$\varphi(x) = \pm\left[\arccos\tanh\left(\frac{x - x_\mathrm{c}}{w/2}\right)\right], \tag{3}$$

with the domain wall center x_c and the domain wall width $w = 2\sqrt{J/K}$, where J is the exchange energy density and K is the effective anisotropy. As described in Ref. [47], Chap. 3.6.1, this simple tanh profile of the magnetization angle, also used for the uniaxial system, shall be sufficient for a qualitative analysis.

IV. DISCUSSION

Overall, the surface magnetic domain structure of Tb films on W(110) closely resembles earlier results obtained on Dy [7]. Our data align with previous reports, indicating that ferromagnetic Tb is magnetized along the $\langle 10\bar{1}0\rangle$ directions [25,29,31]. The direct correlation of topographic and magnetic SP-STM data allows for an evaluation of the influence of various pinning centers. Our results indicate that—even at optimal growth conditions—Tb films with a thickness $\Theta = 20$ AL exhibit numerous structural defects which massively pin the domains during the domain formation process at $T_\mathrm{N,C}$. Hereby, step dislocations and structural boundaries between differently stacked Tb patches are particularly effective. Surface step edges also seem to play a role, though to a lesser extent. As a result of strong pinning, small domains with a lateral size of a few tens of nm form.

With increasing Tb thickness, the density of structural defects rapidly decreases, resulting in larger and larger surface domains. Already at $\Theta = 50$ AL, structural domain boundaries have relaxed and are no longer available for pinning. Instead, only a few double-screw dislocations are observed which appear to pin magnetic domains to a lesser extent. Up to the highest film thickness investigated in this paper, $\Theta = 500$ AL, step dislocations and impurities which both appear as depressions in topographic STM scans remain as acting pinning centers.

Domain wall profiles of a 90-AL Tb film are analyzed in detail in Fig. 5. We find wall thicknesses of $w_{60} \approx 1.4$ nm, $w_{120} \approx 2$–3 nm, and $w_{180} \approx 2$–4 nm for 60°, 120°, and 180° walls, respectively. Especially, for 120° and 180° domain walls, a significant variation of the width by about a factor of 1.5 to 2 is found. Close inspection of the data presented in Figs. 5(b)–5(g) reveals that—irrespective of the total absolute turn angle—domain walls for which the magnetization rotates through the direction antiparallel to the tip magnetization, i.e., panels (b), (d), and (f), are narrower than those where $\vec{m}_\mathrm{s}$ rotates via a path which is aligned with $\vec{m}_\mathrm{t}$.

We ascribe these different apparent wall widths to the dipolar interaction between the Tb-coated tip and the ferromagnetic sample mediated by the stray field. In contrast to antiferromagnetic tips, which exhibit a macroscopically compensated magnetization and therefore allow for a strongly reduced dipolar tip-sample interaction, it is well known that ferromagnetic tips may influence the intrinsic domain structure of the sample [46]. Obviously, a tip which is magnetized antiparallel to the sample, $\vec{m}_\mathrm{s} \upharpoonleft\downharpoonright \vec{m}_\mathrm{t}$ leads to a repulsive interaction; i.e., the domain wall center is initially repelled by the approaching tip. Only if a critical restoring force is reached will the domain wall abruptly pass underneath the tip, resulting in a transition of the $\mathrm{d}I/\mathrm{d}U$ signal which is narrower than the actual domain wall width. In contrast, if $\vec{m}_s \upharpoonleft\!\downharpoonright \vec{m}_t$, the tip will already attract the domain wall center at some distance and drag it until the abovementioned critical force is reached. Therefore, one expects a widening of the apparent domain wall width.

Although the dipolar interaction between the STM tip and the sample inhibits a precise determination of the intrinsic domain wall width of Tb, the abovementioned reasoning implies that the respective intrinsic values must lie between the two extrema we measure in Figs. 5(b)–5(g), i.e., $w_{60} \approx 1.4$ nm, $w_{120} \approx 2.5$ nm, and $w_{180} \approx 3$ nm. These domain wall widths differ significantly from earlier theoretical studies of domain walls for the rare-earth metals Tb and Dy in bulk performed by Egami and Graham [28], who calculated a Bloch domain wall width of 7 nm between ferromagnetic basal planes, where the "spins in each plane are parallel to one another and to the plane of the wall, and the net moment on each plane is rotated progressively about the *c*-axis perpendicular to the wall." Obviously, this theoretical setting is quite different from the domain walls we investigated experimentally. In both cases the magnetization rotates about the *c* axis; i.e., the same component of the magnetocrystalline anisotropy energy density in the basal plane has to be considered. However, our data presented in Fig. 5 reveal that the domain walls observed on the surface of Tb(0001) films are of Néel type, whereas Egami and Graham [28] considered Bloch walls. In most cases Bloch walls are energetically favorable in ferromagnetic bulk materials, as they help to minimize internal magnetic charges [47]. Since SP-STM measurements are highly surface sensitive, we must consider that the surface magnetic anisotropy can differ significantly from bulk properties. It is well-known that Bloch domain walls would generate a stray field at the sample surface which can be avoided by Néel-type walls, resulting in reduced total magnetic energy. Characteristic Néel caps, i.e., bulk Bloch domain walls capped by a Néel-type structure, have been observed in ground-breaking experiments [48,49].

With SP-STM, the differences between these two wall types may be too subtle to detect, as the technique measures the projection of the magnetization vector $\vec{m}_s$ onto $\vec{m}_t$ rather than the magnetization angle itself. Consequently, the slight angular deviation in the tail of the domain wall, characteristic of Néel walls [47], remains below the sensitivity limit of SP-STM. Future research may shine light on the precise spin structure of the Néel cap in Tb films and material-specific parameters, such as the anisotropy energy density or the different components of the magnetic exchange constant.

While the relevant component of the exchange constant for Bloch walls is the one parallel to the *c* axis, $J_\parallel$, for the Néel-type walls we observe the exchange coupling within the basal plane, $J_\perp$, matters. The analysis of spin wave dispersion data measured by inelastic neutron scattering [50,51] suggested $J_\parallel > J_\perp$, in qualitative agreement with our findings.

V. SUMMARY

In this work, we presented a detailed analysis of the magnetic domain structures of Tb(0001) films epitaxially grown on W(110). The measurements were undertaken with spin-polarized scanning tunneling microscopy. With this technique, we were able to map high-resolution magnetic domain structures in the real space of the rare-earth metal Tb. The data reveal a ferromagnetically ordered Tb film with a sixfold symmetry for films thicker than $\Theta > 20$ AL. The data unveiled that most adjacent domains are separated by 60° domain walls, but occasionally 120° and even 180° domain walls could be observed. The analysis of the domain wall profiles led to the assumption that they are of Néel type, with wall thicknesses ranging from $w_{60} \approx 1.4$ nm, $w_{120} \approx 2.5$ nm, and $w_{180} \approx 3$ nm for 60°, 120°, and 180°, respectively. Furthermore, the analysis of the domain wall profiles revealed a rotational-dependent wall thickness, attributed to a dipolar interaction between Tb-covered tips and the stray field of the ferromagnetic Tb sample.

ACKNOWLEDGMENTS

We acknowledge financial support by the Deutsche Forschungsgemeinschaft (DFG, German Research Foundation) through Project No. 510676484 (GZ: BO 1468/29-1) and under Germany's Excellence Strategy through the Würzburg–Dresden Cluster of Excellence on Complexity and Topology in Quantum Matter, ct.qmat (EXC 2147, Project No. 390858490).

[1] R. J. Elliott, Phenomenological discussion of magnetic ordering in the heavy rare-earth metals, Phys. Rev. **124**, 346 (1961).

[2] W. C. Koehler, Magnetic properties of rare-earth metals and alloys, J. Appl. Phys. **36**, 1078 (1965).

[3] S. C. Wu, H. Li, Y. S. Li, D. Tian, J. Quinn, F. Jona, and D. Fort, Surface state on clean Tb(0001), Phys. Rev. B **44**, 13720 (1991).

[4] S. C. Wu, H. Li, Y. S. Li, D. Tian, J. Quinn, F. Jona, D. Fort, and N. E. Christensen, Reexamination of the electron band structure of Tb along the $\Gamma\Delta A$ line, Phys. Rev. B **45**, 8867 (1992).

[5] M. Bode, Spin-polarized scanning tunnelling microscopy, Rep. Prog. Phys. **66**, 523 (2003).

[6] Roland Wiesendanger, Spin mapping at the nanoscale and atomic scale, Rev. Mod. Phys. **81**, 1495 (2009).

[7] S. Krause, L. Berbil-Bautista, T. Hänke, F. Vonau, M. Bode, and R. Wiesendanger, Consequences of line defects on the magnetic structure of high anisotropy films: Pinning centers on Dy/W(110), Europhys. Lett. **76**, 637 (2006).

[8] L. Berbil-Bautista, S. Krause, M. Bode, and R. Wiesendanger, Spin-polarized scanning tunneling microscopy and spectroscopy of ferromagnetic Dy(0001)/W(110) films, Phys. Rev. B **76**, 064411 (2007).

[9] L. Berbil-Bautista, S. Krause, M. Bode, A. Badía-Majós, C. de la Fuente, R. Wiesendanger, and J. I. Arnaudas, Nanoscale spin structures dominated by magnetoelastic interactions around dislocation cores as seen via spin-polarized STM, Phys. Rev. B **80**, 241408(R) (2009).

[10] M. Bode, M. Getzlaff, and R. Wiesendanger, Spin-polarized vacuum tunneling into the exchange-split surface state of Gd(0001), Phys. Rev. Lett. **81**, 4256 (1998).

[11] P. Härtl, M. Leisegang, and M. Bode, Magnetic domain structure of epitaxial Gd films grown on W(110), Phys. Rev. B **105**, 174431 (2022).

[12] U. Kamber, A. Bergman, A. Eich, D. Iusan, M. Steinbrecher, N. Hauptmann, L. Nordström, M. I. Katsnelson, D. Wegner, O. Eriksson, and A. A. Khajetoorians, Self-induced spin glass state in elemental and crystalline neodymium, Science **368**, eaay6757 (2020).

[13] J. Kołaczkiewicz and E. Bauer, The adsorption of Eu, Gd and Tb on the W(110) surface, Surf. Sci. **175**, 487 (1986).

[14] J. Kołaczkiewicz and E. Bauer, Low-energy electron loss spectroscopy of Eu, Gd, and Tb: The valence region, Surf. Sci. **265**, 39 (1992).

[15] E. Navas, K. Starke, C. Laubschat, E. Weschke, and G. Kaindl, Surface core-level shift of $4f$ states for Tb(0001), Phys. Rev. B **48**, 14753 (1993).

[16] J. Kołaczkiewicz and E. Bauer, Low-energy electron-energy-loss spectroscopy of Eu, Gd, and Tb: $5s$ and $5p$ excitations, Phys. Rev. B **47**, 16506 (1993).

[17] F. Hübinger, C. Schüßler-Langeheine, A. V. Fedorov, K. Starke, E. Weschke, A. Höhr, S. Vandré, and G. Kaindl, Temperature-dependent study of the partially filled surface state on Tb(0001), J. Electron Spectrosc. Relat. Phenom. **76**, 535 (1995).

[18] E. Arenholz, E. Navas, K. Starke, L. Baumgarten, and G. Kaindl, Magnetic circular dichroism in core-level photoemission from Gd, Tb, and Dy in ferromagnetic materials, Phys. Rev. B **51**, 8211 (1995).

[19] G. van der Laan, E. Arenholz, E. Navas, Z. Hu, E. Mentz, A. Bauer, and G. Kaindl, Magnetic circular dichroism in $5p$ photoemission from Gd and Tb metal, Phys. Rev. B **56**, 3244 (1997).

[20] R. Kalinowski, L. T. Baczewski, M. Baran, D. Givord, C. Meyer, and J. Raułuszkiewicz, Correlation between magnetic properties and surface structure observed by scanning tunnelling microscopy in Tb epitaxial thin films, Appl. Phys. A **66**, S1205 (1998).

[21] M. Bode, M. Getzlaff, A. Kubetzka, R. Pascal, O. Pietzsch, and R. Wiesendanger, Temperature-dependent exchange splitting of a surface state on a local-moment magnet: Tb(0001), Phys. Rev. Lett. **83**, 3017 (1999).

[22] J. Kołaczkiewicz, Thermal stability of the atomic structure of ultrathin films of Eu, Gd and Tb adsorbed on W(110), Vacuum **56**, 191 (2000).

[23] K. M. Döbrich, G. Bihlmayer, K. Starke, J. E. Prieto, K. Rossnagel, H. Koh, E. Rotenberg, S. Blügel, and G. Kaindl, Electronic band structure and Fermi surface of ferromagnetic Tb: Experiment and theory, Phys. Rev. B **76**, 035123 (2007).

[24] A. Melnikov, A. Povolotskiy, and U. Bovensiepen, Magnon-enhanced phonon damping at Gd(0001) and Tb(0001) surfaces using femtosecond time-resolved optical second-harmonic generation, Phys. Rev. Lett. **100**, 247401 (2008).

[25] J. E. Prieto, G. Chen, A. K. Schmid, and J. de la Figuera, Magnetism of epitaxial Tb films on W(110) studied by spin-polarized low-energy electron microscopy, Phys. Rev. B **94**, 174445 (2016).

[26] K. Göhler, A. B. Schmidt, and M. Donath, Monolayer attenuation length of low-energy electrons in Gd and Tb, J. Vac. Sci. Technol. A **39**, 023205 (2021).

[27] J. Jensen and A. Mackintosh, *Rare Earth Magnetism: Structures and Excitations* (Clarendon Press, Oxford, 1991).

[28] T. Egami and C. D. Graham, Jr., Domain walls in ferromagnetic Dy and Tb, J. Appl. Phys. **42**, 1299 (1971).

[29] J. J. Rhyne, Bulk magnetic properties, in *Magnetic Properties of Rare Earth Metals*, edited by R. J. Elliott (Springer US, Boston, MA, 1972), pp. 129–185.

[30] J. J. Rhyne and A. E. Clark, Magnetic anisotropy of terbium and dysprosium, J. Appl. Phys. **38**, 1379 (1967).

[31] F. J. Darnell, Magnetostriction in dysprosium and terbium, Phys. Rev. **132**, 128 (1963).

[32] D. E. Hegland, S. Legvold, and F. H. Spedding, Magnetization and electrical resistivity of terbium single crystals, Phys. Rev. **131**, 158 (1963).

[33] F. Heigl, J. E. Prieto, O. Krupin, K. Starke, G. Kaindl, and M. Bode, Annealing-induced extension of the antiferromagnetic phase in epitaxial terbium metal films, Phys. Rev. B **72**, 035417 (2005).

[34] Kh. Zakeri, T. R. F. Peixoto, Y. Zhang, J. Prokop, and J. Kirschner, On the preparation of clean tungsten single crystals, Surf. Sci. **604**, L1 (2010).

[35] J. C. Slonczewski, Conductance and exchange coupling of two ferromagnets separated by a tunneling barrier, Phys. Rev. B **39**, 6995 (1989).

[36] T. Miyazaki and N. Tezuka, Giant magnetic tunneling effect in Fe/Al_2O_3/Fe junction, J. Magn. Magn. Mater. **139**, L231 (1995).

[37] D. Wortmann, S. Heinze, Ph. Kurz, G. Bihlmayer, and S. Blügel, Resolving complex atomic-scale spin structures by spin-polarized scanning tunneling microscopy, Phys. Rev. Lett. **86**, 4132 (2001).

[38] H. Li, D. Tian, J. Quinn, Y. S. Li, S. C. Wu, and F. Jona, Structural and electronic properties of ultrathin films of Gd, Tb, Dy, Ho, and Er, Phys. Rev. B **45**, 3853 (1992).

[39] A. Kubetzka, M. Bode, O. Pietzsch, and R. Wiesendanger, Spin-polarized scanning tunneling microscopy with antiferromagnetic probe tips, Phys. Rev. Lett. **88**, 057201 (2002).

[40] The existence of some dendritically shaped indentations signals a tiny ($<3\%$ of the surface area) hydrogen (H) contamination caused by a nonperfectly clean Tb source in the early days of this experimental study. These patches appear dark in the dI/dU map due to the lower density of states of H/Tb(0001), as already observed in earlier studies [11,41–44].

[41] R. Pascal, C. Zarnitz, M. Bode, M. Getzlaff, and R. Wiesendanger, Surface electronic structure of Gd(0001) films on W(110), Appl. Phys. A **65**, 603 (1997).

[42] M. Getzlaff, M. Bode, S. Heinze, R. Pascal, and R. Wiesendanger, Temperature-dependent exchange splitting of the magnetic Gd(0001) surface state, J. Magn. Magn. Mater. **184**, 155 (1998).

[43] M. Getzlaff, M. Bode, and R. Wiesendanger, Hydrogen adsorption on Gd(0001), Surf. Sci. **410**, 189 (1998).

[44] M. Getzlaff, M. Bode, R. Pascal, and R. Wiesendanger, Adsorbates on Gd(0001)—A combined scanning tunneling

microscopy and photoemission study, Phys. Rev. B **59**, 8195 (1999).

[45] See Supplemental Material at http://link.aps.org/supplemental/10.1103/PhysRevB.110.184405 for a detailed analysis of various dI/dU maps and their histograms as well as domain wall profile simulations.

[46] A. Kubetzka, O. Pietzsch, M. Bode, and R. Wiesendanger, Spin-polarized scanning tunneling microscopy study of 360° walls in an external magnetic field, Phys. Rev. B **67**, 020401(R) (2003).

[47] A. Hubert and R. Schäfer, *Magnetic Domains—The Analysis of Magnetic Microstructures* (Springer, Berlin, 2008).

[48] H. P. Oepen and J. Kirschner, Magnetization distribution of 180° domain walls at Fe(100) single-crystal surfaces, Phys. Rev. Lett. **62**, 819 (1989).

[49] M. R. Scheinfein, J. Unguris, R. J. Celotta, and D. T. Pierce, Influence of the surface on magnetic domain-wall microstructure, Phys. Rev. Lett. **63**, 668 (1989).

[50] H. Bjerrum Møller and J. C. Gylden Houmann, Inelastic scattering of neutrons by spin waves in terbium, Phys. Rev. Lett. **16**, 737 (1966).

[51] D. A. Goodings, Exchange interactions and the spin-wave spectrum of terbium, J. Phys. C: Solid State Phys. **1**, 125 (1968).